Journal of Materials Chemistry A

High-efficiency Purification of CH4 and H2 Energy Sources Enabled by a Phosphotungstic Acid-supported Os Single-atom Catalyst

Journal:	*Journal of Materials Chemistry A*
Manuscript ID	TA-ART-08-2023-004850.R1
Article Type:	Paper
Date Submitted by the Author:	16-Oct-2023
Complete List of Authors:	Zhang, Li-long; Northeast Electric Power University, Chemical Engineering Zheng, Ji; Jinan University, Gu, Jinxing; Monash University Huang, Zhuochun; Guizhou University Lu, Linguo; University of Puerto Rico, Department of Chemistry Li, Hu; Guizhou University, State Key Laboratory Breeding Base of Green Pesticide & Agricultural Bioengineering, Key Laboratory of Green Pesticide & Agricultural Bioengineering, Ministry of Education, State-Local Joint Laboratory for Comprehensive Utilization of Biomass, Center for R&D of Fine Chemical Chen, Zhongfang; University of Puerto Rico, Chemistry Yang, Song; Guizhou University, Research and Development of Fine Chemicals

High-efficiency Purification of CH_4 and H_2 Energy Sources Enabled by a Phosphotungstic Acid-supported Os Single-atom Catalyst

Li-Long Zhang,[1†] Ji Zheng,[2†] Jinxing Gu,[3] Zhuochun Huang,[1] Linguo Lu,[4] Hu Li,[1,*] Zhongfang Chen,[4,*] Song Yang,[1,*]

[1] National Key Laboratory of Green Pesticide, Key Laboratory of Green Pesticide and Agricultural Bioengineering, Ministry of Education, State-Local Joint Laboratory for Comprehensive Utilization of Biomass, Center for R&D of Fine Chemicals of Guizhou University, Guiyang, 550025, China

[2] College of Chemistry and Materials Science, Guangdong Provincial Key Laboratory of Functional Supramolecular Coordination Materials and Applications, Jinan University, Guangzhou 510632, China

[3] Department of Chemical & Biological Engineering, Monash University, Clayton Campus, Victoria 3800, Australia

[4] Department of Chemistry, University of Puerto Rico, Rio Piedras Campus, San Juan, PR, USA

[†] Both authors contributed equally to this work.

* Correspondence:

E-mail: hli13@gzu.edu.cn (HL); zhongfang.chen1@upr.edu (ZC); jhzx.msm@gmail.com (SY)

ABSTRACT

Methane (CH_4) and hydrogen (H_2) show promise as low-carbon energy sources, but their impurities, including H_2 and CO, pose challenges for storage and use. To address these challenges, a robust purification protocol for CH_4 and/or H_2, combined with the catalytic conversion of impurities into CO_2 and H_2O, is a compelling solution. In this work, we investigated 11 phosphotungstic acid (PTA)-supported single-atom catalysts (SACs) by density functional theory (DFT) computations. Os_1/PTA SACs exhibited superior catalytic activity, and the ease of oxidation follows the CO > H_2 > CH_4 order. It facilitated efficient purification of CH_4 in solvents such as water, MeOH, and various others. For H_2 purification, Os_1/PTA SACs demonstrated excellent performance in gas, water, and MeOH. Notably, in water and MeOH, it selectively removed CO without consuming H_2 with low free energy barriers. The strong Os-PTA interactions and charge transfer mechanism contributed to its exceptional catalytic activity. Our findings shed light on SAC behavior and their potential for efficient CH_4 and H_2 purification. By addressing impurity challenges and improving clean energy utilization, these findings contribute to the development of sustainable energy technologies.

Keywords: H_2 purification; CH_4 purification; Phosphotungstic acid; Single-atom catalysts; Clean energy utilization

1. Introduction

The urgent need to address global energy and environmental challenges arising from the continuous combustion of fossil fuels has driven the demand for sustainable, safe, and clean energy resources.[1-10] As the principal component of natural gas, methane (CH_4) currently contributes 21.4% to the global primary energy supply.[2] The lower carbon-to-hydrogen (C/H) ratio of natural gas compared to oil and coal positions CH_4 combustion as an effective strategy for mitigating CO_2 emissions, making natural gas a promising alternative energy source in resolving the energy crisis.[4] Notably, the successful exploitation of shale gas has significantly enhanced the availability of natural gas.

However, natural gas, including synthetic natural gas, often contains impurities, mainly H_2 and CO (up to 17.5% and 2.3%, respectively),[9,11,12] which pose significant challenges for practical applications (see Figure 1). Especially, high levels of H_2 impurities render natural gas unsuitable for transportation *via* gas pipelines, as H_2 easily escapes through small openings, leading to material brittleness and potential explosion hazards.[13] In comparison, CH_4 oxidation is quite hard because of the high chemical stability of the inert C-H bonds of CH_4 characterized by a dissociation energy of 104 kcal/mol.[4] Therefore, removing CO and H_2 impurities from CH_4 by oxidation is both feasible and crucial for the effective utilization of natural gas.

Hydrogen (H_2) is another promising future energy candidate due to its zero pollutant emissions and high energy density.[3,14] With approximately 50 million tonnes of H_2 produced annually, H_2 has been extensively used in many industrial processes,

such as hydrogenation and hydrotreating reactions, petroleum refining, and ammonia synthesis.[13] Industrial H_2 production is predominated by water gas shift and steam methane reforming reactions, which result in a considerable amount of CO impurities (typically 1%).[15] These CO impurities must be effectively eliminated in H_2 applications, particularly for fuel cells and ammonia synthesis, as the catalysts used are highly sensitive to CO.[3,16] An efficient strategy for H_2 purification is the using small amounts of O_2 (approx 1%). This process selectively oxidizes CO without affecting H_2, aiming at achieve over 50% selectivity of oxygen to CO_2 while reducing the CO concentration to 50 ppm.[17] However, realizing such high selectivity and oxidation rates (~10^6 times faster for CO than H_2) in practical catalysts remains a significant challenge.[3] Therefore, the quest for highly efficient, cost-effective, stable, and long-lasting catalysts for CO and H_2 oxidation, particularly in CO PROX for H_2 applications, persists as an ongoing challenge.

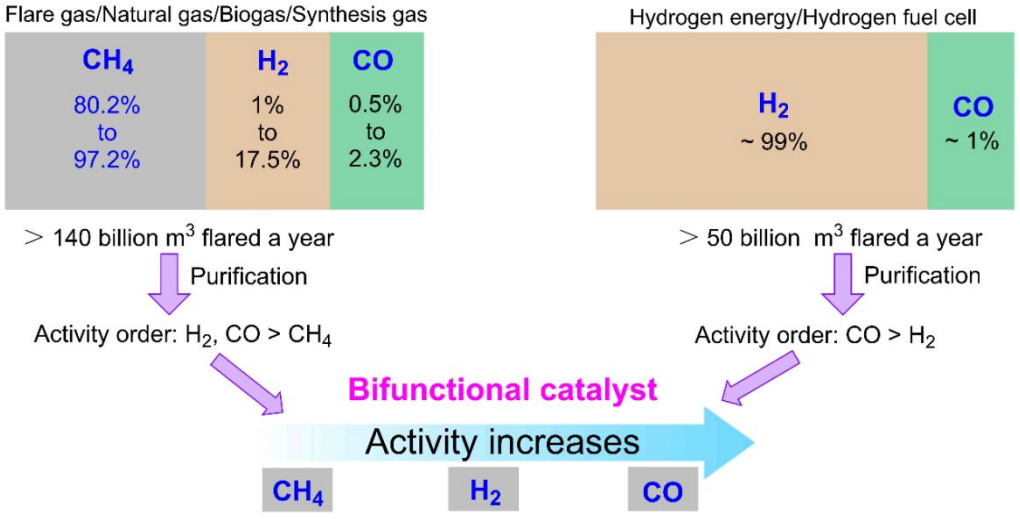

Figure 1. Schematic illustration of catalytic CH_4 and H_2 purification.

Single-atom catalysts (SACs), known for their maximal atom utilization, are highly active for CO and H_2 oxidation, making them ideal for CO PROX and a top choice for CH_4 and H_2 purification.[16,18-24] Unfortunately, the fabrication of robust SACs is not easy as the metal single atoms are highly active and generally unstable when exposed to environmental stress,[25] and thus tend to sinter to form nanoparticles and clusters.[26]

To address this issue, Keggin-type polyoxometalates (POMs) have been identified as top-performing materials for loading SACs , thanks to the "small island effect",[27] that prevents diffusion and modifies electronic properties. Among others, the phosphotungstic acid (PTA)-based SACs, such as Rh_1/PTA developed by Yan's group, were first applied for CO oxidation by O_2, exhibiting a temperature-dependent catalytic activity according to the *in-situ* spectroscopy results.[28,29] They proposed a Mars van Krevelen mechanism (CO adsorption strength far higher than O_2), which was subsequently confirmed by computational investigations.[19,22] Previous studies have demonstrated the role of water in accelerating CO PROX by suppressing competing H_2 oxidation.[17,30-32] POMs can be dissolved in organic and aqueous solvents, allowing their use in homogeneous and heterogeneous catalytic systems.[18,26,33,34] Despite extensive research on Keggin POM-based metal SACs in CO oxidation, the influence of solvents has been largely overlooked.

Reactive oxygen species (ROS), including hydroxide radical, singlet O_2 ($^1O_2$), O_3, and H_2O_2, represent a unique class of environment-friendly chemicals with stronger oxidability compared to ground-state O_2.[35-37] Recent decades have thus witnessed

remarkable performances of ROS in various fields, such as catalysis, synthesis, environmental pollution control, and chemical biology.[36,38,39] However, the generation of hydroxide radical and $^1O_2$ requires energy expenditure (light, electricity, or heat), while O_3 and H_2O_2 are significantly more expensive in comparison to O_2.[38,39] Thus, the pursuit of highly efficient catalysts for O_2 activation is of utmost importance and highly desirable.

The single O atom adsorbed on metal or non-metal atoms is also called ROS due to its higher catalytic performance than adsorbed ground-state O_2.[23,40] Typically, the dissociation of O_2 molecules occurs on the two or more adsorbed sites of nanomaterials.[41-46] However, in the case of SACs, which possess only one adsorption site, studies on O_2 dissociation over single-atom systems have been limited. Our previous investigations revealed that upon consecutive dissociation of two N_2O molecules over Ru_1/PTA, Os_1/PTA, and Ir_1/PTA SACs in the gas phase, two isolated O atoms (referred to as dissociative adsorption O_2: $^dO_2$) were formed instead of ground-state dioxygen molecule (referred to as molecular adsorption O_2: $^mO_2$) in these three systems.[20 47]Moreover, the dual single O atoms in the Os_1/PTA system could realize cooperative catalysis for H_2. The reaction between the triplet $^mO_2$ and singlet CO and H_2, resulting in the production of singlet CO_2 and H_2O, is spin-forbidden, leading to poor catalytic performance. In contrast, the singlet $^dO_2$ species display high activity in such reactions, as confirmed by our previous studies.[20] However, despite the crucial role that solvents play in the formation of $^dO_2$ over a catalytic system, this aspect has not received much attention to our best knowledge. From a materials design perspective,

the formation of $^{d}O_2$ over a catalytic system in various solvents holds significant importance for achieving high catalytic activity.

In this work, we performed systematic DFT computations to evaluate the feasibility of maintaining the dual dissociative O_2 species ($^{d}O_2$) over a range of M_1/PTA SACs (M = Mn, Fe, Co, Ni, Ru, Rh, Pd, Re, Os, Ir, and Pt) in gas and 12 commonly used solvents including THF,[48] water, CCl_4, PhH (Ph = -C_6H_5), PhCl, PhMe, acetone (ACE), MeOH, EtOH, MeCN, dimethyl sulfoxide (DMSO) and $CHCl_3$, aiming at developing a generally viable strategy for CH_4 and H_2 purification. Our computational results show that the high activity of dual ROS can be maintained in Re_1/PTA and Os_1/PTA SACs across all tested cases. Furthermore, electronic structure analyses indicate that the activity follows the order of Os_1/PTA > Re_1/PTA (catalysts) and CO > H_2 > CH_4 (reactants). Our subsequent comprehensive computational investigations confirmed these speculations. The Os system exhibits exceptional catalytic activity, enabling H_2 purification in gas, water, and MeOH, as well as CH_4 purification in water, THF, CCl_4, PhH, PhCl, PhMe, ACE, MeOH, MeCN, DMSO, and $CHCl_3$. Furthermore, the in-depth kinetic and thermodynamic analysis further support the viability of bifunctional Os catalysts for the purification of H_2 and CH_4 gases (see Figure 1).

2. Computational methods

Gaussian 16 suite of the program was used for all the quantum chemistry calculations.[49] The Multiwfn software was utilized for Hirshfeld charge calculation and Mayer bond order (MBO) analysis.[50,51] The Hirshfeld population,[52] spin density and

molecular orbital contribution were also performed by Multiwfn and drawn by VMD software.[53] The thermodynamic parameters at different temperatures were obtained by the Shermo program.[54] For geometry optimization, all the structures were fully relaxed in the gas phase using the M06L method,[55] a local meta-GGA exchange-correlation functional. The all-electron basis set 6-31G(d)[56] was used for the non-metal atoms and the pseudopotential basis set LANL2DZ[57] was employed for the metal atoms. The harmonic vibrational frequencies were calculated at normal temperature and pressure (298.15 K and 1 atm) using the same computational level as geometry optimization. The M06L functional has shown an excellent performance in research of large-scale systems, thermochemistry, thermochemical kinetics and covalent interaction.[55] Additionally, Liu's group has confirmed that this function represents a powerful tool for predicting accurate geometries, kinetics, thermochemistry, vibrational frequency, reaction mechanism, and other properties of PTA.[18]

The optimized minima were confirmed by the absence of imaginary frequencies while each transition state was confirmed by only one imaginary frequency. The transition state models were further confirmed by intrinsic reaction coordinate (IRC) calculations. For obtaining more accurate electronic energies, higher-level calculations were performed using the polarization and diffusion 6-31+G(d,p)[40,58] basis set for all non-metal atoms and SDD[59] pseudopotential basis set for metal atoms. Therefore, the gas-phase Gibbs free energies are the sum of single-point energy at M06L/6-31+G(d,p): SDD and the Gibbs free energy corrections (including zero-point energy and thermal contribution to the free energy) at M06L/6-31G(d): LANL2DZ.

The SMD[60] implicit solvent model has been applied to describe the 12 solvent effects by M05-2X/6-31G(d) (LANL2DZ on metal). The solvation energy (ΔE_{sol}) is calculated as follows: $\Delta E_{sol} = E_{sol} - E_{vac}$, where E_{sol} and E_{vac} represent the single-point energies of the solute in solvent (based on the optimized structure in vacuum) and that in vacuum. Herein, all the discussed energies are the changes of Gibbs free energy with the implicit solvent model (gas-phase Gibbs free energy + ΔE_{sol}) at room temperature. The rationale behind the application of the implicit solvation model is provided in the Supporting Information.

The calculated adsorption energy of the molecule ($\boldsymbol{E}_{ad}$) is defined: $\boldsymbol{E}_{ad}(A) = \boldsymbol{E}_{A\text{-}M} - \boldsymbol{E}_{M} - \boldsymbol{E}_{A}$, where $\boldsymbol{E}_{A\text{-}M}$, $\boldsymbol{E}_{M}$, and $\boldsymbol{E}_{A}$ represent the total energies of the catalyst after adsorption, the clean catalyst, and the free molecule, respectively. For calculated free energy profiles, the activation barrier ($\boldsymbol{E}_{a}$) and the reaction energy ($\boldsymbol{E}_{r}$) are defined: $\boldsymbol{E}_{a} = \boldsymbol{E}_{TS} - \boldsymbol{E}_{IS}$ and $\boldsymbol{E}_{r} = \boldsymbol{E}_{FS} - \boldsymbol{E}_{IS}$, where IS, TS and FS represent the initial state, transition state, and final state, respectively. Thus, the positive and negative values of $\boldsymbol{E}_{ad}/\boldsymbol{E}_{r}$ indicate an endothermic and exothermic process, respectively. The rate constants were calculated by the classical transition state theory based on thermodynamic quantities formalism: $k = \sigma\kappa\frac{k_b T}{h}\exp(-\frac{Ea}{RT})$, in which k, σ, κ, k_b, T, h, E_a, and R represent reaction rate, degeneracy (default = 1), transmission coefficient (default = 1), Boltzmann constant, reaction temperature, Plank constant and free energy barrier.[61,62]

3. RESULTS AND DISCUSSION

3.1. Screening eligible catalysts by examining the ROS formation

The geometry optimization process considers the influence of spin multiplicity, and Table S1 provides the spin multiplicities for various configurations, including pristine SACs and their complexes interacting with reactants (CH_4, CO, molecular adsorption $^{m}O_2$, and dissociative adsorption $^{d}O_2$) and products (H_2O, CH_3OH, CO_2). The surface oxygen atoms in the Keggin-type PTA structure can be categorized into three types: terminal (O_t), bridging two W atoms (O_b), and corner (O_c).[63] The catalytic activity of the O_t atoms is negligible due to intense $O_t \cdots W$ interactions (Mayer bonding order (MBO) = 1.773). Notably, the O_b and O_c atoms exhibit different behaviors in catalytic activity, with O_c atoms being more prominent than O_b atoms ($\angle$W-O_c-W = 126.57° vs $\angle$W-O_b-W = 152.14°). Hence, the O_b and O_c atoms are configurationally nonequivalent, and it is expected that their catalytic activities behave differently when different metal atoms are anchored to form SACs.

Though POMs, such as PTA, contain a large number of surface oxygen atoms, their practical applications in catalysis are severely limited due to their relatively low melting point (<100 ^{o}C).[29] Previous research has shown that POM-supported SACs (M_1/POM) greatly activate the O_b and O_c atoms SACs.[20] Therefore, the catalytic performance of the pristine PTA support will not be considered in this work.

Numerous experimental and theoretical studies have demonstrated that the metal cation forms one-to-one binding with the surface of PTA,[28,29] with the 4-fold hollow site being the most stable anchored site for SACs (Fig. 2a). However, the reaction between the triplet $^{m}O_2$ and the singlet CO and H_2 to produce singlet CO_2 and H_2O is

spin-forbidden, resulting in a poor activity. Luckily, the $^{d}O_2$ species remains in the singlet state, leading to a high catalytic performance for both reactions.

Considering the enhanced catalytic activity of ROS, we began our investigation by determining whether the formation of $^{d}O_2$ is possible over various SACs, specifically M_1/PTA (M = Mn, Fe, Co, Ni, Ru, Rh, Pd, Re, Os, Ir, and Pt), in both gas phase and 12 commonly used liquid solvents, namely, THF, water, CCl_4, PhH, PhCl, PhMe, ACE, MeOH, EtOH, MeCN, DMSO, and $CHCl_3$. Because only the Re_1/PTA and Os_1/PTA SACs have dissociative O_2 adsorption in the gas phase and all the solvents considered based on our DFT calculations (Figure 2b and Figures S1-S3), we will focus on these two catalysts in this work.

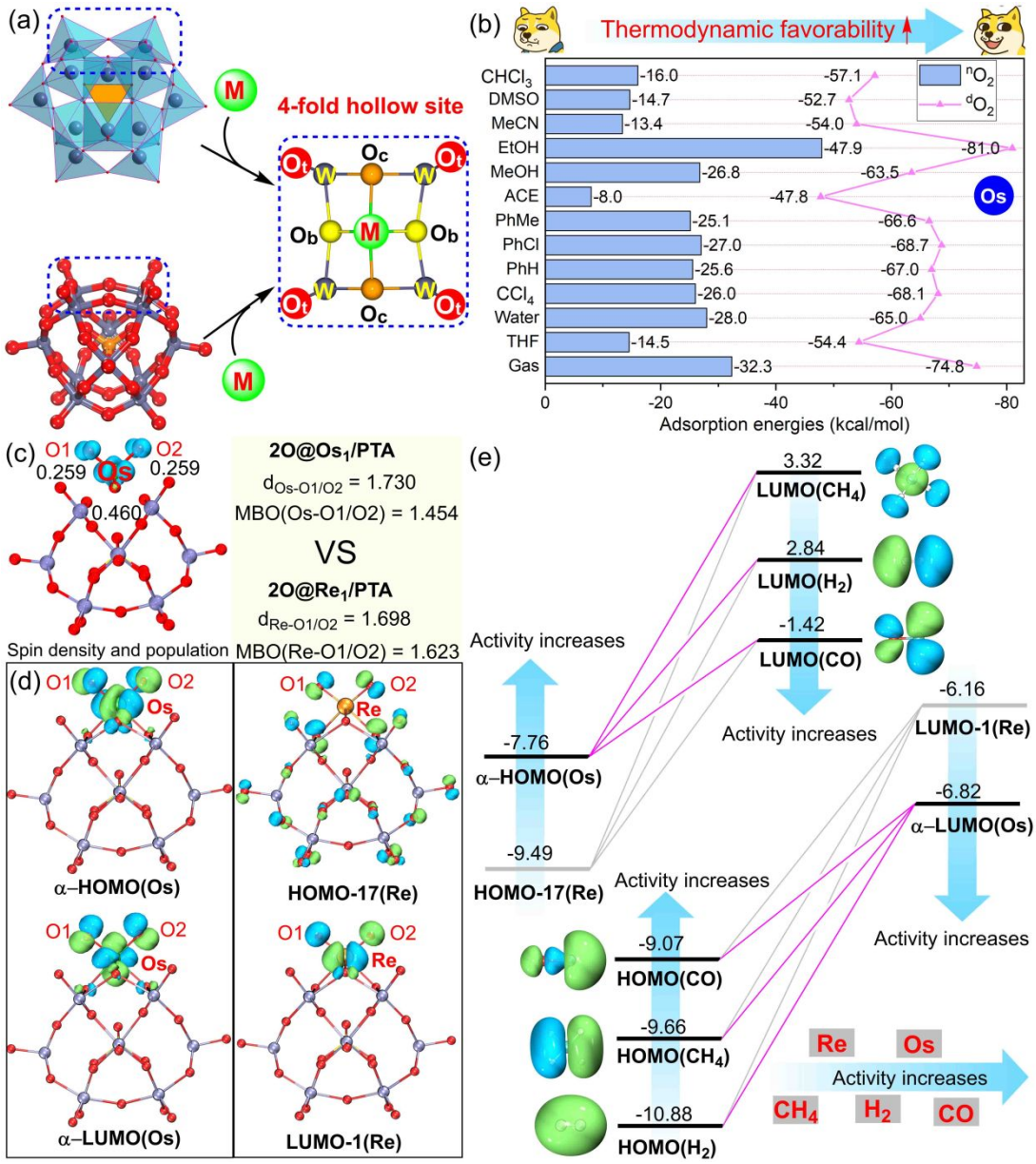

Figure 2. (a) Keggin-type PTA structure and four-fold hollow site for binding a single metal atom. (b) Adsorption energies of one O_2 for molecular and dissociative adsorption over Os_1/PTA SACs. (c) spin-density isosurfaces (isovalue = 0.05) for $2O@Os_1$/PTA (green: positive spin-density; blue: negative spin-density) with corresponding spin population; structure comparison between $2O@Os_1$/PTA and $2O@Re_1$/PTA. (d) Shapes of ROS-relevant molecular orbitals (isovalue = 0.05) of $2O@Os_1$/PTA and $2O@Re_1$/PTA. (e) Energy levels (eV) and shapes (isovalue = 0.05) of molecular

orbitals for ROS-relevant 2O@Os_1/PTA, 2O@Re_1/PTA, and free CH_4, H_2, and CO molecules.

3.2. Estimating the catalytic activity of Re_1/PTA and Os_1/PTA SACs by geometric and electronic structures

We first examine the structural features of these two catalysts. The optimization calculations show that the M−O1/O2 distances in 2O@Os_1/PTA and 2O@Re_1/PTA systems are 1.730/1.730 and 1.698/1.698 Å, respectively, and the corresponding MBO values are 1.454/1.454 and 1.623/1.623, respectively (Fig 2c), indicating that the Os-O bond is much easier to cleave. Therefore, the ROS in the Os system should have a higher catalytic performance compared to that of the Re system.

Then, we investigated the electronic structures of Re_1/PTA and Os_1/PTA SACs. To evaluate their oxidative capacity, we calculated the Hirshfeld charges of oxygen atoms in 2O@Os_1/PTA and 2O@Re_1/PTA systems (Figure S4). The less negative charge of the two ROS in both systems indicated their stronger oxidative ability than the oxygen atom in PTA support.

Furthermore, the Hirshfeld population combined spin density plot of 2O@Os_1/PTA (doublet state) showed high spin density residing on the O1/O2 atoms (0.277/0.277), which could be considered free radical species $(2O)^-$, again suggesting highly reactive properties of the ROS. Due to the singlet state of 2O@Re_1/PTA, no spin density was located in ROS atoms in the Re system, also indicating their low catalytic performance.

To obtain further insight into the activity of the two catalytic systems ($2O@Os_1$/PTA and $2O@Re_1$/PTA) and the three target molecules (CO, H_2, and CH_4), we performed a detailed orbital analysis. The ROS-relevant highest occupied molecular orbitals (HOMOs) of $2O@Os_1$/PTA and $2O@Re_1$/PTA are α-HOMO（Os) and HOMO-17(Re), respectively. Note that the term "HOMO(Os)" refers to the HOMO of the Os-catalyst, and similar notations are used for other molecular orbital names. The corresponding ROS-relevant lowest unoccupied molecular orbitals (LUMOs) are α-LUMO(Os) and LUMO-1(Re), respectively (Fig. 2d). It can be found that α-HOMO（Os), α-LUMO(Os) and LUMO-1(Re) are mainly composed of metal d-orbitals and O1/O2 p-orbitals, which represent the antibonding interaction between Os(Re) and O1/O2 atoms.

The activation processes for CO, H_2, and CH_4 molecules on the ROS site involve electron transfer between the three target molecules and the ROS-relevant catalysts ($2O@Os_1$/PTA and $2O@Re_1$/PTA). According to molecular orbital (MO) theory, the different activity for catalysts (Os and Re) and target molecules (CO, H_2, and CH_4) can be attributed to their different energy levels (Fig 2e). The occupied ROS-relevant molecular orbitals (MOs) α-HOMO(Os) and HOMO-17(Re) could provide electrons to the LUMO(CO), LUMO(H_2), and LUMO(CH_4) with the antibonding character of C-O, H-H, and C-H, which can significantly weaken the C-O, H-H, and C-H bonding (Fig 2e). Meanwhile, the occupied MOs HOMO(CO), HOMO(H_2), and HOMO(CH_4) with C-O, H-H, and C-H bonding characters could transfer electrons to α-LUMO(Os) and LUMO-1(Re), further weakening the C-O, H-H, and C-H bonding. Based on the

molecular orbital energy levels of ROS-relevant catalysts and three target molecules, we thus presume that Os_1/PTA outperforms Re_1/PTA with a reactivity order of CO > H_2 > CH_4, providing a remarkable opportunity to realize efficient purification protocols for CH_4 and H_2.

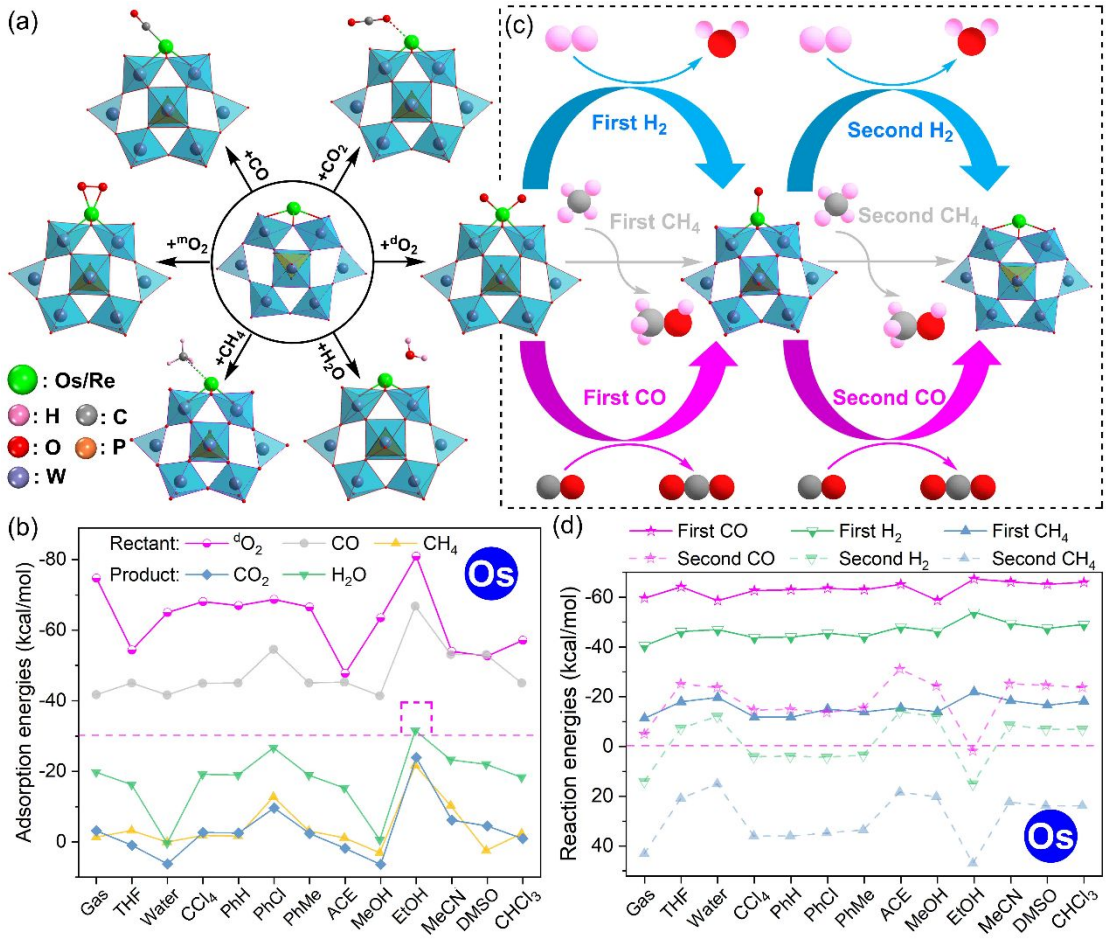

Figure 3. Optimized geometries of catalysts with adsorbed molecules: CH_4, CO, H_2O, CO_2, as well as molecularly and dissociatively adsorbed O_2 (a). Adsorption energies of the reactant and product over Os_1/PTA (b). Catalytic pathways of CO, H_2, and CH_4 oxidation over Os_1/PTA (c). Reaction energies for the first and second steps over Os_1/PTA in the gas phase and 12 solvents (d).

3.3. Catalyst screening by computing adsorption energy and reaction energy

The ability of a catalyst to effectively capture and retain reactant molecules around its active adsorption site significantly impacts its catalytic performance.[23] The adsorption energy ($\boldsymbol{E}_{ad}$) of the reactant plays a crucial role in determining the reaction mechanism, which is the first and pivotal step within a catalytic cycle.[22,23] Furthermore, excessively high $\boldsymbol{E}_{ad}$ of the product could suppress the catalyst activity and even lead to catalyst deactivation.[64,65] Thus, Figure 3a presents the optimized structures that yield the energetically most favorable configurations for each reactant ($^{m}O_2$, $^{d}O_2$, CO, and CH_4) and product (CO_2 and CH_3OH) over Os_1/PTA and Re_1/PTA SACs, Figure 3b illustrates the adsorption energies in the gas phase, while Figure S5a presents the corresponding adsorption energies in 12 common liquid solvents.

A comparison of the adsorption energies in both gas and 12 different solvents reveals a consistent trend for the recants and products. Additionally, it demonstrates a significant influence on the gas phase adsorption energy. The weak adsorption energies of products indicate that they are unlikely to poison the catalyst (water adsorption is slightly strong in the EtOH solvent for the Os system). The more negative adsorption energies of $^{d}O_2$ compared to other gases in both Os_1/PTA and Re_1/PTA SACs suggest the presence of dual ROS under all conditions. However, in Re systems, the $^{d}O_2$ adsorption is excessively strong (ranging from -81.0 to -133.6 kcal/mol, Figure S5a) compared to the Os systems (ranging from -47.8 to -74.8 kcal/mol, Figure 3b), leading to the formation of strong metal-oxygen bonds (Figure 2c), and thus raising concerns regarding catalyst poisoning.

Figure 3c illustrates the catalytic pathways for the oxidation of CO, H_2, and CH_4 over the active intermediate $2O@M_1$/PTA (M = Os and Re). Figure 3d provides the corresponding reaction energies ($\boldsymbol{E}_r$) for the first and second steps over Os_1/PTA, while Figure S5b displays the $\boldsymbol{E}_r$ values for Re_1/PTA. The trend of variation in $\boldsymbol{E}_r$ for both steps remains similar in the two systems under different conditions. Notably, for the second step of CO, H_2, and CH_4 oxidation in the Re system, all the $\boldsymbol{E}_r$ values are nearly positive (Figure S5b), indicating a very low catalytic activity. Consequently, the Re_1/PTA SACs will not be considered, and we will focus on Os_1/PTA SACs in the following sections.

3.4. Catalytic performance towards CO, H_2, and CH_4, and the feasibility of concurrent purification of CH_4 and H_2 over Os_1/PTA SACs

Wc calculated the $\boldsymbol{E}_r$ values for the oxidation of CO, H_2, and CH_4 molecules in both gas phase and 12 solvents over the Os system (Figure 3d). For the first step, $\boldsymbol{E}_r$ decreases in the following order: CO (from -58.7 to -67.3) > H_2 (from -40.5 to -54.0) > CH_4 (from -11.4 to -21.9). This trend indicates that the catalytic performance towards CO is better than H_2, and H_2 is easier to oxidize than CH_4. For the second step, CO oxidation is potentially feasible in most cases (except in EtOH due to a positive $\boldsymbol{E}_r$ value); H_2 oxidation may only be feasible in solvents such as THF, water, ACE, MeOH, MeCN, DMSO, and $CHCl_3$ (with negative $\boldsymbol{E}_r$ values). In contrast, the positive $\boldsymbol{E}_r$ value for the second step of CH_4 oxidation suggests that this reaction is very difficult to occur. Overall, these data confirm the viability of concurrent purification of CH_4 and H_2 by

selectively oxidizing CO. In the following sections, we will carefully examine the CO and H_2 oxidation pathways over Os_1/PTA SACs, compare the catalytic reactivity (or ease of oxidation) of these two gases, and provide a comprehensive analysis of the reaction mechanisms.

3.5. CO oxidation pathway over Os_1/PTA SACs

Firstly, we examined CO and H_2 oxidation over Os_1/PTA SACs separately due to the complexity of their respective reaction mechanisms. Figure 4a illustrates the main catalytic cycle involved in CO oxidation catalyzed by Os_1/PTA, while the corresponding calculated free energy profiles in the gas phase and 11 solvents (based on the $\boldsymbol{E}_r$ results in Figure 3d) are presented in Figure 4b (for water and MeOH) and Figure S6 (for other cases), respectively.

The CO oxidation reaction initiates with the adsorption of $^dO_2$ onto the Os_1/PTA surface, then the free CO molecule simultaneously attacks the two ROS (^{Os}**TS1**), leading to the formation of a stable intermediate (***CO_3**). The first CO_2 molecule is produced (***CO_2 + O***) by passing a transition state (^{Os}**TS2**). Concomitantly with the desorption of CO_2, a single ROS (**O***) adsorbed onto the Os center undergoes a reaction with the adsorbed second CO molecule (***CO + O***, ^{Os}**TS3**, and ***CO_2**). Finally, the desorption of the second CO_2 molecule completes the regeneration of the Os_1/PTA SACs (*****).

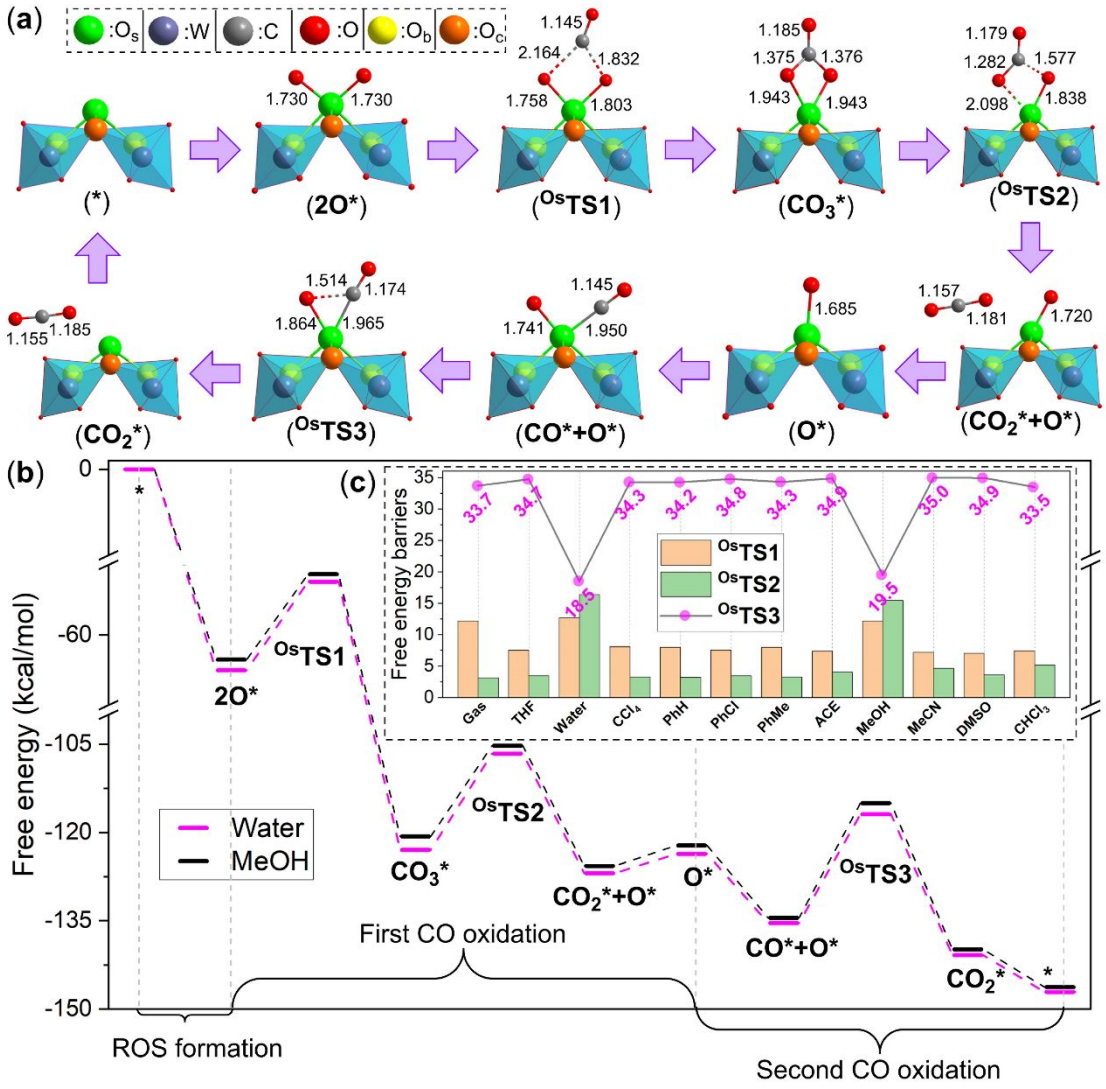

Figure 4. (a) The main catalytic cycle of CO oxidation catalyzed by Os_1/PTA SACs (the simplified model is provided for visual clarity). (b) Calculated free energy profiles (in kcal/mol) of CO oxidation over Os_1/PTA SACs in water and MeOH. (c) Free energy barriers of ^{Os}**TS1**, ^{Os}**TS2**, and ^{Os}**TS3** in gas and 11 solvents.

The main catalytic cycle can be divided into three parts: ROS formation (from * to **2O***), the first CO oxidation (from **2O*** to **O***), and the second CO oxidation (from **O*** to *). The second CO oxidation is speculated to be a rate-determining step (RDS) due to the shorter Os-O bond in **O*** (1.69 Å) compared to that in **2O*** (1.73 Å). The

calculated free profiles in both the gas phase and 11 solvents exhibit a consistent trend of energy variation (Figure 4b and Figure S6). Among the three transition states, ^{Os}**TS3** exhibits the highest energy barrier, indicating its role as the RDS (Figure 4c). The calculated energy barriers indicate that CO oxidation is feasible in all cases, with lower barriers in water and MeOH (18.5 and 19.5 kcal/mol, respectively) compared to other solvents (ranging from 33. 5 to 35.0 kcal/mol). Interestingly, the combined values of ^{Os}**TS1**, ^{Os}**TS2**, and ^{Os}**TS3** in each case are nearly identical (Figure S7). Consequently, the activation energies are relatively small in water and MeOH, as the values of ^{Os}**TS1**, ^{Os}**TS2**, and ^{Os}**TS3** are very close in both solvents. This finding is very similar to electrocatalytic nitrogen (N_2) and oxygen evolution reactions,[66,67] where improved catalytic performance is associated with the progressively closer values of the $\boldsymbol{E}_r$ for each elementary step.

Figure S8 presents two possible side paths, namely, P1 and P2, in which the first CO molecule only attacks one O atom (**2O***, ^{Os}**TS4**, ***CO_2** + **O***), and the second free CO molecule directly attacks the O atom without pre-adsorption (**O***, ^{Os}**TS5**, ***CO_2**). For the first CO oxidation, the energy barrier value of ^{Os}**TS4** is not always greater than the maximum of ^{Os}**TS1** and ^{Os}**TS2** (much smaller in water, Figure S9), indicating that P1 could be the main reaction pathway in water. However, the rather high free energy barriers of ^{Os}**TS5** (Figure S10) indicate that P2 is not feasible. Thus, the RDS remains unchanged (always ^{Os}**TS3**) for CO oxidation across all tested cases. The lower $\boldsymbol{E}_a$ of ^{Os}**TS3** compared with that of ^{Os}**TS5** will be discussed in more detail below.

3.6. H_2 oxidation pathway over Os_1/PTA SACs

Figure 5a illustrates the dominant reaction path for H_2 oxidation over Os_1/PTA SACs. The corresponding free energy profiles in seven solvents, based on the $\boldsymbol{E}_r$ results of Figure 3d, are shown in Figure 5b (water and MeOH) and in Figure S11 (for other cases).

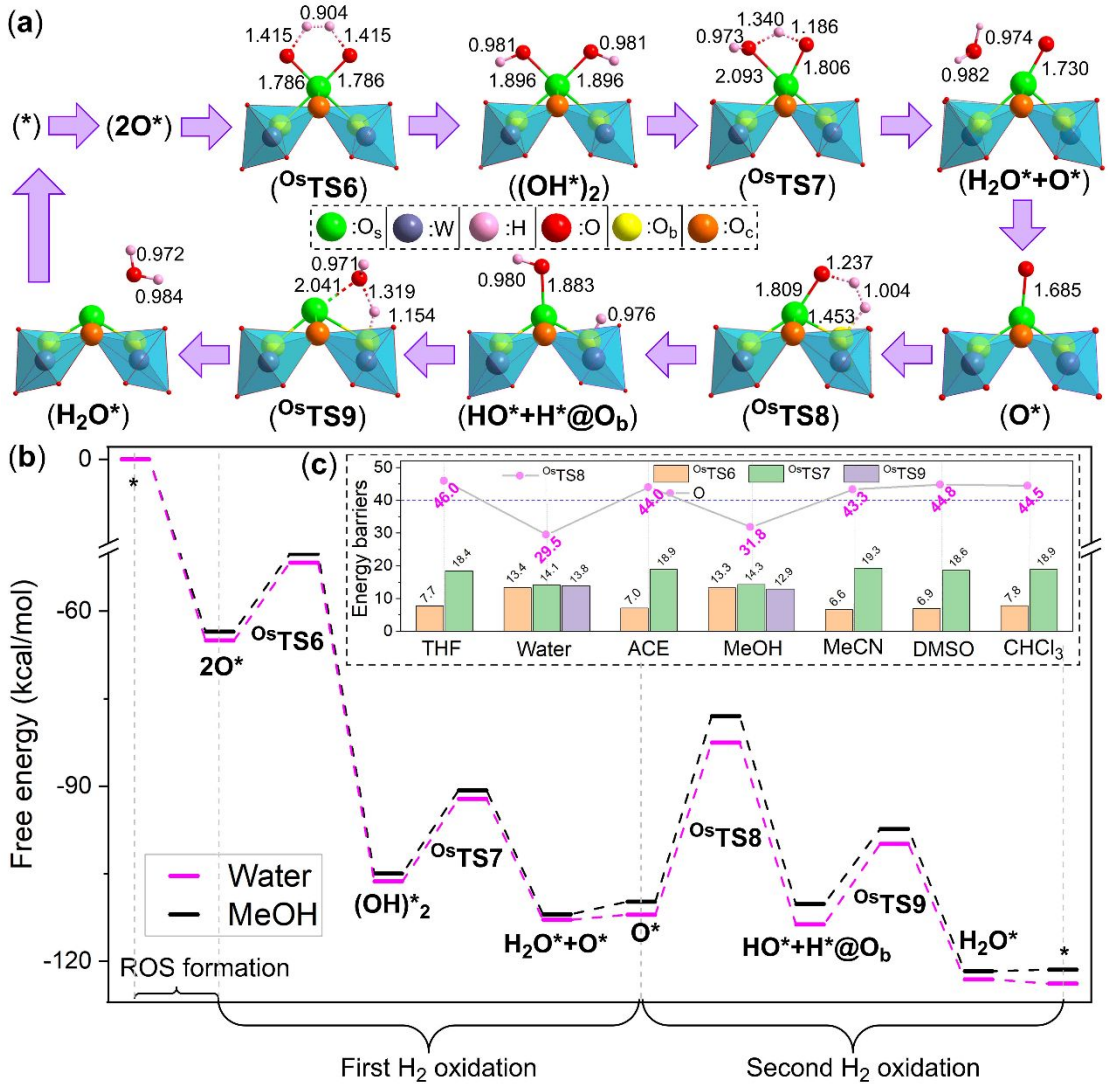

Figure 5. (a) Main catalytic cycle of Os_1/PTA SACs-catalyzed H_2 oxidation (simplified model for visual presentation). (b) Calculated free energy profiles (in kcal/mol) of H_2

oxidation over Os_1/PTA SACs via O_b site in water and MeOH. (c) Free energy barriers of ^{Os}**TS6**, ^{Os}**TS7**, ^{Os}**TS8**, and ^{Os}**TS9** in seven solvents.

After $^{d}O_2$ adsorption, the simultaneous attack of two hydrogen atoms of the free H_2 molecule on the two ROS (^{Os}**TS6**) leads to the formation of a stable intermediate (**(OH*)$_2$**). By passing a transition state (^{Os}**TS7**), an H_2O molecule is produced (**H_2O*** + **O***). With the desorption of CO_2, the first H_2 oxidation is completed, and a bare single ROS (**O***) is generated. The relatively low energy barriers of ^{Os}**TS6** and ^{Os}**TS7** indicate that H_2 oxidation is significantly facilitated in the seven solvents. Subsequently, the second free H_2 molecule interacts with both the single ROS and a surface oxygen atom of PTA. Our previous studies showed that the coordinated O_b and O_c atoms are chemically nonequivalent and their catalytic performance always varies from case to case. Thus, both the second H_2 dissociation pathways through O_b and O_c sites were explored. In the O_b site pathway, the formation of a metastable intermediate (**HO*** + **H*@O$_b$***) is first generated by passing ^{Os}**TS8**, followed by the production of the second H_2O molecule (**H_2O***) via ^{Os}**TS9**. However, the energy barriers of ^{Os}**TS8** in THF, ACE, MeCN, DMSO, and $CHCl_3$ are excessively high (Figure 5c), rendering these cases unsuitable for further detailed investigation.

Comparing all the energy barriers for H_2 dissociation over the O_b site (Figure 5c) revealed that this process is limited to water and MeOH, with relatively moderate energy barriers of the RDS (^{Os}**TS8**, 29.5 and 31.8 kcal/mol, respectively). In contrast, the high energy barriers observed for H_2 dissociation over the O_c site (Figure S12)

indicate that this step is unfeasible (**^{Os}TS10**, from 47.0 to 50.9 kcal/mol) at normal temperatures.

Notably, the free H_2 molecule has the ability to directly attack the two bound OH species (Figure S13a, **(OH*)$_2$**, **^{Os}TS11**, **(H$_2$O*)$_2$**) without being restricted by the E_r values set for the second H_2 oxidation (Figure 3d). The calculated energy barriers of **^{Os}TS11** (Figure S13b) indicate that this pathway is likely feasible in nine solvents. Consequently, H_2 oxidation can occur in water and MeOH through a stepwise oxidation path (RDS: 29.5 and 31.8 kcal/mol). Additionally, in THF, CCl_4, PhH, PhCl, PhMe, ACE, MeCN, DMSO, and $CHCl_3$, H_2 oxidation can proceed through a direct double H_2 oxidation path (RDS: from 24.6 to 30.7 kcal/mol).

3.7. Assessment of the reactivity of H_2 and CO

The purification of CH_4, specifically the removal of H_2 and CO, is feasible in several solvents, including THF, water, CCl_4, PhH, PhCl, PhMe, ACE, MeOH, MeCN, DMSO, and $CHCl_3$, as summarized in Figure 6a. This feasibility is based on the reasonable energy barrier of RDS for CO and H_2 oxidation. In the gas, water, and MeOH solvents, the CO oxidation is kinetically more favorable compared to H_2 oxidation, as evidenced by its significantly lower activation energy (E_a, 33.7 vs 39.7, 18.5 vs 29.5, and 19.5 vs 31.8 kcal/mol, respectively).

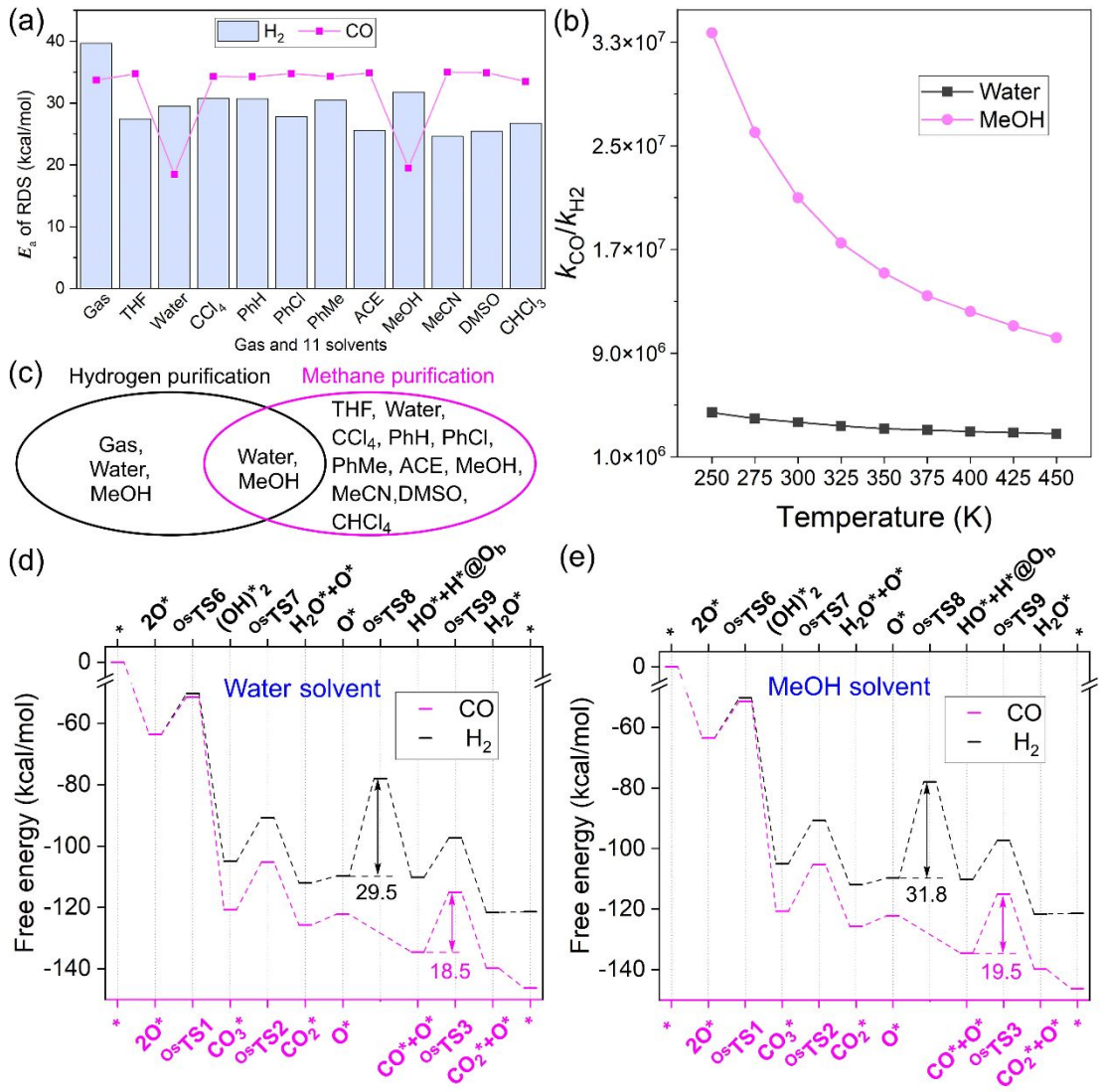

Figure 6. (a) Free energy barriers of the rate-determining step for CO and H_2 oxidation. (b) Ratio of reaction rates for CO and H_2 in water and MeOH. (c) Identification of suitable solvents for H_2 and CH_4 purification. (d) and (e) Free energy profiles of CO and H_2 oxidation following the favorable pathway in water and MeOH.

The key factor in achieving CO PROX (preferential oxidation of CO in the presence of H_2) is the difference in reaction rate (k) between CO and H_2 oxidation. Previous studies have determined that in order to prevent H_2 from being consumed, the k of CO oxidation should be at least 10^6 times higher than that of H_2 oxidation. [3] Based

on the formula (computational details), the k value strongly depends on temperature and $\boldsymbol{E}_a$ (also affected by temperature).

Table S2 presents the $\boldsymbol{E}_a$ values of the RDS for CO and H_2 oxidation in gas, water, and MeOH at various temperatures (from 250 to 350 K). Increasing the temperature slightly decreases the $\boldsymbol{E}_a$ for CO oxidation by ca. 0.1 kcal/mol, while significantly increases the $\boldsymbol{E}_a$ for H_2 oxidation (i.e., 5.6 kcal/mol in gas, and 5.7 kcal/mol in water and MeOH). The $\boldsymbol{E}_a$ of H_2 oxidation in gas becomes prohibitively large (from 38.4 to 43.9 kcal/mol), making this process unrealistic. Thus, CO PROX in H_2 could be achievable in a gas environment.

The reaction rates for CO and H_2 in water and MeOH, summarized in Table S3, indicate that both reactions occur at sufficiently high rates. As shown in Figure 6c, the ratios of the reaction rates for CO and H_2 (k_{CO}/k_{H2}) in both water and MeOH are greater than 1×10^6 across the studied temperature range. Therefore, no H_2 will be consumed during the CO PROX process by regulating the amount of added O_2, as supported by previous studies.[3,17,68]

To further evaluate the thermodynamic feasibility of H_2 purification (CO PROX in excess H_2), we analyzed the most favorable pathways for CO and H_2 oxidation in water and MeOH (as H_2 oxidation is kinetically forbidden in gas) together (Figure S15). The corresponding free energy profiles are compared in Figure 6d and 6e, respectively.

The lower curves of the free energy profiles for CO oxidation in water and MeOH indicate that the CO PROX process investigated in this study is thermodynamically favorable. This finding confirms that H_2 purification in gas, water, and MeOH is indeed

achievable. Therefore, it can be concluded that Os_1/PTA is an efficient catalyst for H_2 purification (in gas, water, and MeOH, respectively) and CH_4 purification (in THF, water, CCl_4, PhH, PhCl, PhMe, ACE, MeOH, MeCN, DMSO, and $CHCl_3$, respectively). Furthermore, the catalyst exhibits bifunctional activity in water and MeOH environments.

3.8. Role of Os active center and PTA support on catalytic activity

The geometries and electronic structures of the catalyst and support are well-known to influence the catalytic performance. Investigating the role of the Os center and PTA support could provide insights into the findings and reveal the fundamentally associative nature of the entire catalytic system. Selected geometric and electronic structure parameters for PTA, **2O***, **O***, and **CO*+O*** are presented in Table 1, and the corresponding structure diagram is shown in Figure 7a.

Comparing **O*** with **2O***, it is found that the double ROS in **2O*** is more prone to dissociate from the catalyst surface due to its longer Os-ROS bond (1.730 vs 1.685 Å) and smaller MBO value (1.454 vs 1.732). A spin density analysis revealed a significant spin density on the double ROS in **2O***, whereas almost no spin polarization is observed at the single ROS in **O*** (Figure 7a). Thus, the double ROS moiety can be regarded as an oxy-radical, as further supported by the Hirshfeld spin population values (0.554 vs 0.03). Moreover, the strong synergy of the double ROS significantly enhances the catalytic activity. As a result, **2O*** exhibits higher catalytic activity for both CO and H_2 oxidation than **O***, in line with previous results (Figures 4 and 5).

Table 1. Selected bond lengths (Å) and angles (deg), Hirshfeld charges (*q*, e), and Hirshfeld spin populations (ρ) and Mayer bond orders (MBO) of PTA, 2O*, O*, and CO*+O*.

Parameters	PTA	**2O***	**O***	**CO*+O***
$d_{(Os\text{-}O1/O2)}$		1.730	1.685	1.741
MBO $_{(Os\text{-}O1/O2)}$		1.454	1.732	1.518
ρ (O1 + O2)		0.518	0.033	0.489
∠W-O_b-W	152.20		146.64	
∠W-O_c-W	126.59		117.83	
$d_{W\text{-}Ob}$	1.924		2.044	
$d_{W\text{-}Oc}$	1.932		2.131	
MBO $_{(W\text{-}Ob)}$	0.705		0.399	
MBO $_{(W\text{-}Oc)}$	0.739		0.430	
$d_{Os\text{-}Ob}$			2.018	
$d_{Os\text{-}Oc}$			2.050	
MBO $_{(Os\text{-}Ob)}$			0.537	
MBO $_{(Os\text{-}Oc)}$			0.626	
ρ (O_b)			0.085	
ρ (O_c)			-0.001	
q (Os)			0.684	0.631
q (O1)			-0.172	-0.168

To investigate the underlying reasons for the different activities between O_b and O_c in the **O*** structure, we analyzed the corresponding geometric and electronic structure parameters here. The bond distances/MBO of W-O_b and W-O_c in **O*** were compared to those in the clean PTA, and the angles of W-O_b/O_c-W were also examined, as shown in Table 1.

It is observed that the bond distances of W-O_b and W-O_c in **O*** are significantly longer and shorter, respectively, compared to those in the clean PTA structure. In addition, the angles of W-O_b/O_c-W in O* are decreased. These findings indicate that both coordinated oxygen atoms are activated.

Furthermore, in the **O*** structure, the longer $d_{W\text{-}Ob}$/$d_{Os\text{-}Ob}$ (along with smaller MBO) compared with $d_{W\text{-}Oc}$/$d_{Os\text{-}Oc}$ indicate that the O_b atom possesses better catalytic activity,

which is further supported by the spin population value (0.085 vs -0.001) and the corresponding spin density distribution (Figure 7b).

Previous studies indicated that the structure is more stable when the adsorbed and reacting molecules lie in the plane consisting of an anchoring metal and two coordinated O_b atoms, with O_b closer to ROS than O_c.[19,21,22] In line with these findings, our analysis confirmed the completion of H_2 dissociation by O_b atoms, rather than O_c atoms, as evidenced by the comparison of the energy barrier values of ^{Os}**TS8** and ^{Os}**TS10** (E_a in Figure 5c vs Figure S12b).

In the **O*** structure, the single ROS exhibits weak activity, primarily due to its short $d_{Os\text{-}O1}$ (large MBO = 1.732) and negligibly spin density (and population) on the single ROS (Figure 7b). Therefore, the direct attack of free CO onto the single ROS is extremely difficult, as indicated by the high E_a of ^{Os}**TS5** (Figure S10).

However, when a CO molecule is adsorbed (**CO*+O***), there is a significant charge redistribution on both ROS and Os center. The charge on ROS changes from -0.172 to -0.168, and the charge on the Os center changes from 0.684 to 0.631. This charge redistribution leads to modification in the electronic structure and geometric rearrangement. Notably, the activation of ROS is evident from the increased spin density (Figure 7c) and spin population (from 0.033 to 0.489) upon the transition from from **O*** to **CO*+O***. This activation of ROS is further supported by the larger Os-ROS bond (1.741 vs 1.685 Å), smaller MBO (1.518 vs 1.732), and the lower energy barrier for ^{Os}**TS3** compared to ^{Os}**TS5**.

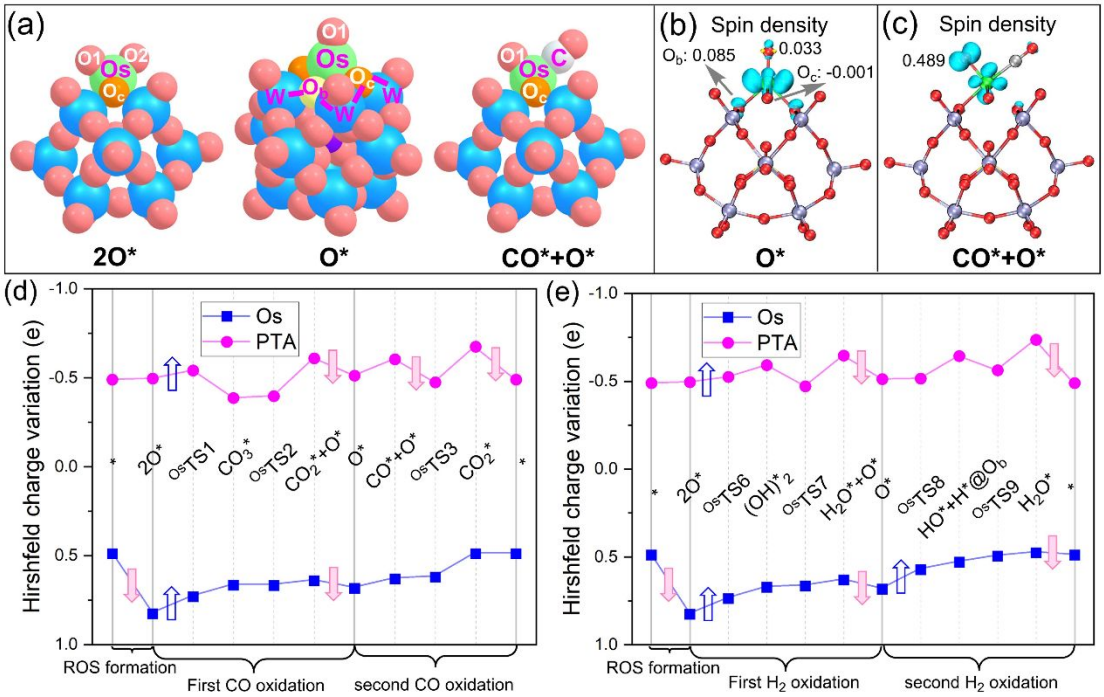

Figure 7. (a) Structure diagram illustrating the configuration of **2O***, **O***, and **CO*+O*** (b) and (c) Spin density distribution (isovalue = 0.05) of **O*** and **CO*+O***. **(d)** and (e) Variation in Hirshfeld charges of the Os center and PTA support during CO and H_2 oxidation (in gas) along their respective most favorable reaction pathways. Blue and pink arrows represent the electron inflow and outflow, respectively.

To further comprehend the role of Os center and PTA support, we examined the variations in Hirshfeld charges for CO and H_2 oxidation in water and MeOH along their most favorable pathways (Figure 7d and 7e). Throughout the entire catalytic reactions involved in CO and H_2 oxidations, notable changes in the charge distribution on PTA are observed. It is well-established that polyoxometalates (POMs) exhibit the ability to self-correct, enabling them to attain a stable configuration with minimal structural modifications upon gaining or losing electrons. This property contributes to the favorable kinetics and thermodynamics observed in each elementary reaction step, as

depicted in Figures 6d and 6e. The strong synergy between the Os center and PTA support plays a crucial role in facilitating these catalytic processes.

The PTA support not only serves as an anchor for the Os SACs, but also plays an important role in modifying their catalytic properties via the metal-support charge transfer and interaction. During the ROS formation process, the Os center acts as the sole electron donor, transferring electrons to the antibonding orbitals of the two Os-ROS moieties (Figure 2d). This electron transfer considerably activates the adsorbed $^{d}O_2$. However, a different situation arises during the second CO oxidation (**^{Os}TS3**), in which electron donation for the catalytic reaction comes solely from the PTA support.

Both the Os center and the PTA support act as electron donors during the adsorption processes of CO and H_2 molecules. In the case of the Eley-Rideal mechanism, where the free gas directly attacks the adsorbate, such as in CO and H_2 oxidations (**^{Os}TS1**, **^{Os}TS6**, and **^{Os}TS8**), both the Os center and the PTA support contribute to activating the ROC by donating electrons into the antibonding orbitals of the Os-ROS bond.

The above findings indicate a cooperative charge transfer mechanism between the Os SACs and the PTA support along the reaction pathways. In the subsequent steps following the intermediate formation (**CO_2*** to **^{Os}TS2**, **(OH)*$_2$** to **^{Os}TS7**, and **HO* + H*@O_b*** to **^{Os}TS9**), the charge on the Os center shows minimal variation, while a significant increase is observed for the PTA support. The electrons are thus transferred primarily from the support to the adsorbates through the Os center, highlighting the role of Os SACs as efficient electron transport bridges in these processes.

It is well known that studying variations in Hirshfeld charges (q, e) and spin populations (ρ, e) of catalysts can yield valuable insights into catalytic reactions.[69] To investigate the influence of solvents on the metal active site, we compared the Hirshfeld charges and spin populations of the Os center in the Os_1/PTA catalyst in the gas phase and across different solvents (see Table S4 for detailed data). The charges of the Os center in both water and MeOH are significantly more positive than those in all other solvents, except for MeCN, where the charge is lower than that in water but higher than in MeOH. The same trend was observed for the spin populations of the Os site across various solvents. Thus, the transfer of the outermost electrons of the Os center into the C=O bond is enhanced in these solvents, facilitating the activation of the C=O bond and thereby enhancing the catalytic performance of Os_1/PTA SACs in both water and MeOH solvents.

4. Conclusions

Modern society faces significant challenges in the areas of health, energy, and the environment. In order to address these challenges, this study employed density functional theory (DFT) calculations to investigate a series of M_1/PTA single-atom catalysts (SACs) for the purification of CH_4 and H_2 in both gas phase and 12 commonly used solvents. We found that the dissociation of O_2 occurs exclusively on the surfaces of Os and Re SACs, leading to the formation of highly reactive oxygen species. The catalytic performance of the studied catalysts was predicted to follow the order of Os_1/PTA > Re_1/PTA, with CO oxidation exhibiting the highest reactivity, followed by

H_2 and CH_4. Such a reactivity trend makes it possible to simultaneously purify CH_4 and H_2. Further computations revealed that Os_1/PTA is an efficient bifunctional catalyst that can enable the purification of CH_4 in THF, water, CCl_4, PhH, PhCl, PhMe, ACE, MeOH, MeCN, DMSO, and $CHCl_3$, as well as the purification of H_2 in gas, water, and MeOH. Especially in water and MeOH, Os SACs demonstrate remarkable catalytic performance in CO PROX with low energy barriers of 18.5 and 19.5 kcal/mol, respectively, while ensuring no consumption of H_2. Through electronic structure analyses, it has been determined that the Os center and PTA support not only play an essential role in activating dissociated O_2 but also serve as electron transfer mediators.

By overcoming obstacles related to impurities in the purification of CH_4 and H_2 energy sources, these findings make a valuable contribution to advancing sustainable energy technologies. The results of this study offer promising prospects for the development of efficient and environmentally friendly energy purification processes, paving the way for the realization of a sustainable energy system.

Conflict of Interest

The authors declare that they have no known competing financial interests or personal relationships that could have appeared to influence the work reported in this paper.

Acknowledgments

This study was financially supported in China by the Guizhou Provincial S&T Project (ZK[2022]011, 2018[4007]) and in the USA by the Department of Energy,

Office of Basic Energy Sciences under Award Number DE-SC0023418. We thank the computing support of the State Key Laboratory of Public Big Data, Guizhou University.

References

1. L. Hu, Y. W. Fang, F. Y. Qin, X. Cao, X. X. Zhao, Y. B. Luo, D. V. M. Repaka, W. B. Luo, A. Suwardi, T. Soldi, U. Aydemir, Y. Z. Huang, Z. Liu, K. Hippalgaonkar, G. J. Snyder, J. W. Xu and Q. Y. Yan, *Nat. Commun.*, 2021, **12**, 10.
2. M. Ma, B. J. Jin, P. Li, M. S. Jung, J. I. Kim, Y. Cho, S. Kim, J. H. Moon and J. H. Park, *Adv. Sci.*, 2017, **4**, 8.
3. T. Whittaker, K. B. S. Kumar, C. Peterson, M. N. Pollock, L. C. Grabow and B. D. Chandler, *J. Am. Chem. Soc.*, 2018, **140**, 16469-16487.
4. V. C. C. Wang, S. Maji, P. R. Y. Chen, H. K. Lee, S. S. F. Yu and S. I. Chan, *Chem. Rev.*, 2017, **117**, 8574-8621.
5. Z. Liang, T. Li, M. Kim, A. Asthagiri and J. F. Weaver, *Science*, 2017, **356**, 298-301.
6. Y. Q. Su, J. X. Liu, I. A. W. Filot, L. Zhang and E. J. M. Hensen, *ACS Catal.*, 2018, **8**, 6552-6559.
7. Y. Q. Su, I. A. W. Filot, J. X. Liu and E. J. M. Henseng, *ACS Catal.*, 2018, **8**, 75-80.
8. V. L. Sushkevich, D. Palagin, M. Ranocchiari and J. A. van Bokhoven, *Science*, 2017, **356**, 523-527.
9. D. Kiefer, M. Merkel, L. Lilge, M. Henkel and R. Hausmann, *Trends Biotechnol.*, 2021, **39**, 397-411.
10. Z. Zhong, W. Ren and S. Wang, *J. Mater. Chem. A*, 2023, DOI: 10.1039/d3ta03172a.
11. W. S. Lin, J. X. Xu, L. Zhang and A. Z. Gu, *Int. J. Hydrog. Energy*, 2017, **42**, 18417-18424.
12. M. Flores-Granobles and M. Saeys, *Green Chem.*, 2023, DOI: 10.1039/d3gc01237a.
13. N. Armaroli and V. Balzani, *ChemSusChem*, 2011, **4**, 21-36.
14. D. Wu, S. T. King, N. Sadique, L. Ma, S. N. Ehrlich, S. Ghose, J. Bai, H. Zhong, S. Yan, D. C. Bock, E. S. Takeuchi, A. C. Marschilok, L. M. Housel, L. Wang and K. J. Takeuchi, *J. Mater. Chem. A*, 2023, **11**, 16279-16292.
15. S. S. Wong, R. Y. Shu, J. G. Zhang, H. C. Liu and N. Yan, *Chem. Soc. Rev.*, 2020, **49**, 5510-5560.
16. B. T. Qiao, A. Q. Wang, X. F. Yang, L. F. Allard, Z. Jiang, Y. T. Cui, J. Y. Liu, J. Li and T. Zhang, *Nat. Chem.*, 2011, **3**, 634-641.
17. P. Landon, J. Ferguson, B. E. Solsona, T. Garcia, A. F. Carley, A. A. Herzing, C. J. Kiely, S. E. Golunski and G. J. Hutchings, *Chem. Commun.*, 2005, **3387**, 3385-3387.

18. C. G. Liu, M. X. Jiang and Z. M. Su, *Inorg. Chem.*, 2017, **56**, 10496-10504.
19. C. G. Liu, L. L. Zhang and X. M. Chen, *Dalton Trans.*, 2019, **48**, 6228-6235.
20. C. G. Liu, Y. J. Chu, L. L. Zhang, C. Sun and J. Y. Shi, *Environ. Sci. Technol.*, 2019, **53**, 12893-12903.
21. L. L. Zhang, X. M. Chen and C. G. Liu, *Inorg. Chem.*, 2019, **58**, 5221-5229.
22. L. L. Zhang, M. J. Sun and C. G. Liu, *Mol. Catal.*, 2019, **462**, 37-45.
23. F. Y. Li, Y. F. Li, X. C. Zeng and Z. F. Chen, *ACS Catal.*, 2015, **5**, 544-552.
24. S. J. Park, T. H. Nguyen, D. T. Tran, V. A. Dinh, N. H. Kim and J. H. Lee, *Energy Environ. Sci.*, 2023, DOI: 10.1039/d3ee01314f.
25. J. Wang, Z. Zhang, W. He, Z. Wang, S. Weng, Q. Li, X. Wang, S. Barg, L. Chen, H. Li and F. Wu, *J. Mater. Chem. A*, 2023, **11**, 10239-10253.
26. H. Yan, X. X. Zhao, N. Guo, Z. Y. Lyu, Y. H. Du, S. B. Xi, R. Guo, C. Chen, Z. X. Chen, W. Liu, C. H. Yao, J. Li, S. J. Pennycook, W. Chen, C. L. Su, C. Zhang and J. Lu, *Nat. Commun.*, 2018, **9**, 9.
27. M. Hulsey, J. G. Zhang and N. Yan, *Adv. Mater.*, 2018, **30**, 9.
28. M. J. Hulsey, B. Zhang, Z. R. Ma, H. Asakura, D. A. Do, W. Chen, T. Tanaka, P. Zhang, Z. L. Wu and N. Yan, *Nat. Commun.*, 2019, **10**, 10.
29. B. Zhang, H. Asakura and N. Yan, *Ind. Eng. Chem. Res.*, 2017.
30. J. Saavedra, H. A. Doan, C. J. Pursell, L. C. Grabow and B. D. Chandler, *Science*, 2014, **345**, 1599-1602.
31. E. Quinet, L. Piccolo, F. Morfin, P. Avenier, F. Diehl, V. Caps and J. L. Rousset, *J. Catal.*, 2009, **268**, 384-389.
32. A. U. Nilekar, S. Alayoglu, B. Eichhorn and M. Mavrikakis, *J. Am. Chem. Soc.*, 2010, **132**, 7418-7428.
33. M. D. Tzirakis, I. N. Lykakis and M. Orfanopoulos, *Chem. Soc. Rev.*, 2009, **38**, 2609-2621.
34. I. Efremenko and R. Neumann, *J. Am. Chem. Soc.*, 2012, **134**, 20669-20680.
35. Y. Zhao, C. T. Shao, Z. X. Lin, S. J. Jiang and S. Q. Song, *Small*, 2020, **16**, 5.
36. S. Y. Zuo, Z. Y. Guan, F. Yang, D. S. Xia and D. Y. Li, *J. Mater. Chem. A*, 2022, **10**, 10503-10513.
37. M. Bilal, A. Altaf, E. Bint-E-Khalid, H. K. Zafar, N. Tahir, A. Nafady, M. A. Wahab, S. S. A. Shah, T. Najam and M. Sohail, *RSC Adv.*, 2023, **13**, 23547-23557.
38. K. J. Moor, M. Schmitt, P. R. Erickson and K. McNeill, *Environ. Sci. Technol.*, 2019, **53**, 8078-8086.
39. J. Ding, Y. J. Yao, J. W. Li, Y. Y. Duan, J. R. Nakkala, X. Feng, W. B. Cao, Y. C. Wang, L. J. Hong, L. Y. Shen, Z. W. Mao, Y. Zhu and C. Y. Gao, *Small*, 2020, **16**, 9.
40. M. J. Frisch, J. A. Pople and J. S. Binkley, *J. Chem. Phys.*, 1984, **80**, 3265-3269.
41. Zhu, Lee, Lee and Frauenheim, *Phys. Rev. Lett.*, 2000, **85**, 2757-2760.
42. Z. Feng, B. Zhang, R. Li, F. Li, Z. Guo, S. Zheng, G. Su, Y. Ma, Y. Tang and X. Dai, *J. Power Sources*, 2023, **558**.
43. Z. Feng, Z. Yang, X. Meng, F. Li, Z. Guo, S. Zheng, G. Su, Y. Ma, Y. Tang and X. Dai, *J. Mater. Chem. A*, 2022, **10**, 4731-4738.

44. Y. Tang, W. Chen, M. Zhao, J. Shi, Y. Cui, Z. Li, Z. Wang, Z. Feng and X. Dai, *Fuel*, 2023, **332**.
45. Y. Tang, J. Shi, W. Chen, Y. Li, H. Tian, Y. Cui, Z. Wang, Z. Feng and X. Dai, *Fuel*, 2022, **319**.
46. Z. Feng, Y. Tang, Y. Ma, Y. Li, Y. Dai, W. Chen, G. Su, Z. Song and X. Dai, *Int. J. Hydrog. Energy*, 2021, **46**, 5378-5389.
47. L.-L. Zhang, Y. Su, D. Chen, H. Wu, F. Xu, H. Li and S. Yang, *Inorganic Chemistry Frontiers*, 2023, **10**, 1838-1851.
48. X. Shen, Y. Xiong, F. Yu and J. Ma, *J. Mater. Chem. A*, 2023, DOI: 10.1039/d3ta02715e.
49. M. Testa, G. Iuliano, E. Marino, C. Buongiovanni, F. Paolercio, A. Trapanese, P. Mortow, M. J. Frisch, G. W. Trucks, H. B. Schlegel, G. E. Scuseria, M. A. Robb, J. R. Cheeseman, G. Scalmani, V. Barone, B. Mennucci and G. A. Petersson, *Gaussian 16 A.03*, 2016.
50. T. Lu and F. W. Chen, *J. Comput. Chem.*, 2012, **33**, 580-592.
51. B. A. Sorenson, L. U. Yoon, E. Holmgren, J. J. Choi and P. Clancy, *J. Mater. Chem. A*, 2021, **9**, 3668-3676.
52. T. Lu and F. W. Chen, *J. Theor. Comput. Chem.*, 2012, **11**, 163-183.
53. W. Humphrey, A. Dalke and K. Schulten, *J. Mol. Graph.*, 1996, **14**, 33.
54. T. Lu and Q. X. Chen, *Comput. Theor. Chem.*, 2021, **1200**, 8.
55. Y. Zhao and D. G. Truhlar, *J. Chem. Phys.*, 2006, **125**, 194101.
56. R. Ditchfield, W. J. Hehre and J. A. Pople, *J. Chem. Phys.*, 1971, **54**, 724.
57. P. J. Hay and W. R. Wadt, *J. Chem. Phys.*, 1985, **82**, 270-283.
58. P. C. Hariharan and J. A. Pople, *Theor Chem Acc*, 1973, **28**, 213--222
59. S. Grimme, J. Antony, S. Ehrlich and H. Krieg, *J Chem Phys*, 1994, **100**, 7535.
60. A. V. Marenich, C. J. Cramer and D. G. Truhlar, *J. Phys. Chem. B*, 2009, **113**, 6378-6396.
61. X. Liu, Z. Y. Yang, R. D. Zhang, Q. S. Li and Y. P. Li, *J. Phys. Chem. C*, 2012, **116**, 20262-20268.
62. S. Ketrat, T. Maihom, S. Wannakao, M. Probst, S. Nokbin and J. Lirntrakul, *Inorg. Chem.*, 2017, **56**, 14005-14012.
63. V. W. Day and W. G. Klemperer, *Science (New York, N.Y.)*, 1985, **228**, 533-541.
64. H. Tanaka, H. Nishikawa, T. Uchida and T. Katsuki, *J. Am. Chem. Soc.*, 2010, **132**, 12034-12041.
65. Z. Y. Qi, C. X. Xiao, C. Liu, T. W. Goh, L. Zhou, R. Maligal-Ganesh, Y. C. Pei, X. L. Li, L. A. Curtiss and W. Y. Huang, *J. Am. Chem. Soc.*, 2017, **139**, 4762-4768.
66. C. Y. Ling, L. Shi, Y. X. Ouyang, X. C. Zeng and J. L. Wang, *Nano Lett.*, 2017, **17**, 5133-5139.
67. J. X. Zhao and Z. F. Chen, *J. Am. Chem. Soc.*, 2017, **139**, 12480-12487.
68. P. Lakshmanan, J. E. Park and E. D. Park, *Catal. Surv. Asia*, 2014, **18**, 75-88.
69. Q. Dang, S. Tang, T. Liu, X. Li, X. Wang, W. Zhong, Y. Luo and J. Jiang, *J. Phys. Chem. Lett.*, 2021, **12**, 8355-8362.